Journal of Materials Chemistry A

ROYAL SOCIETY OF CHEMISTRY

PAPER

View Article Online
View Journal

Check for updates

Cite this: DOI: 10.1039/d6ta00897f

Failure mechanisms of aluminum alloy foil anodes in lithium-ion batteries governed by composition and cell design

Caitlin Trejo and Arumugam Manthiram *

Received 29th January 2026
Accepted 5th May 2026

DOI: 10.1039/d6ta00897f

rsc.li/materials-a

Aluminum alloy foil anodes have emerged as a promising class of materials for enabling increased energy density in lithium-ion batteries. However, the complex degradation mechanisms are not fully understood. In this work, aluminum alloyed with 1 wt% alloying elements (Si, Cu, or Mg) in $LiFePO_4$||Al alloy full cells is investigated to uncover the relationship between composition, the negative/positive (N/P) ratio, and the mode of degradation. We show that the alloying element and N/P ratio dictate cycle life performance and the dominant mode of failure. Regardless of alloy composition, at a high N/P ratio (>4), diffusional trapping serves as the primary mode of degradation. Conversely, with a low N/P ratio (<4), the mode of degradation varies based on the alloying element. Diffusional trapping dominated degradation can be characterized by a low first-cycle efficiency (FCE), capacity gain through cycling, improved cycling stability, and structural stability. Pulverization dominated failure is defined by a higher FCE, improved capacity retention at the expense of cycle life, and severe fracturing that results in a porous structure. Understanding these structure–performance relationships provides a roadmap for the rational design of Al foil anodes with improved performance in practical cells.

Introduction

Lithium-ion batteries (LIBs) have revolutionized modern society by enabling technologies, such as portable devices, and are now transforming the transportation sector.[1] To address the rising demand, the development of next-generation LIB materials must focus on increasing energy density, while reducing cost.[2,3] Aluminum (Al) foil anodes have attracted attention as a competitive alternative to the current industry standard, graphite. Al foil anodes enable up to a ~40% increase in energy density, while improving safety, due to their combination of high theoretical volumetric (1411 *vs.* 719 mAh cm^{-3}) and gravimetric (993 *vs.* 372 mAh g^{-1}) capacities and low operating voltage (0.38 *vs.* 0.1 V).[4–9] A recent study has reported the formation of Li-rich phases (Li_3Al_2 and $Li_{2-x}Al$) at room temperature, which may enable a significantly higher capacity (2000 mAh g^{-1}).[10]

Additionally, Al foil anodes reduce manufacturing cost and support large-scale manufacturing by eliminating the need for binders and current collectors, coupled with Al being low cost and abundant.[11–13] A modified cell design has the potential to reduce both the manufacturing costs and energy consumption, as powder-slurry steps account for ~35% of the manufacturing costs and ~50% of the energy consumption.[14,15] Use of recycled aluminum can further reduce energy consumption, requiring only 5% of the energy needed for primary aluminum production.[16]

However, despite these benefits, Al foil anodes are limited by rapid capacity fade during cycling. Pulverization and diffusional trapping are the two mechanisms attributed to the poor cycle life. Al foils undergo an α-Al/β-LiAl phase transformation during charge/discharge, which causes a large volume change (~100%).[17] The repeated expansion and contraction induce cracking, which leads to pulverization of the structure.[18] Pulverization leads to capacity loss by disruption of electronic pathways and excessive growth of the solid electrolyte interphase (SEI).[19,20] Diffusional trapping occurs during discharge, when the surface of the foil becomes passivated with α-Al, leaving LiAl ionically isolated from the electrolyte.[21] Mitigation strategies for these degradation modes have been proposed (prelithiation, electrolyte design, and microstructural modification), but have only focused on alleviating pulverization. Therefore, the relationship linking the Al foil structure and the occurrence of both the failure mechanisms (pulverization and diffusional trapping) remains misunderstood.[22–24]

Recently, there has been growing interest in understanding the microstructural evolution of Al foils during formation and cycling.[25–27] It has been shown that nucleation is a critical determinant of the LiAl microstructure. Increasing the grain boundary density in the pristine Al foil results in more uniform and evenly distributed nucleation, thereby enhancing structural integrity during cycling.[28] Potentiostatic formation with a high

Materials Science and Engineering Program, Walker Department of Mechanical Engineering, The University of Texas at Austin, Austin, TX 78712, USA. E-mail: manth@austin.utexas.edu

overpotential produces small, uniform LiAl islands on the surface during nucleation.[29] As the foil is further lithiated, the small islands transform into a columnar structure, which can reduce diffusional trapping limitations indicated by the increase in the first-cycle efficiency (FCE).[30] Our previous work revealed that capacity loss in high-purity Al (99.99%, 4N Al) foil anodes is caused by the interaction of the two degradation modes, which are highly dependent on cell design.[31] The capacity ratio of the negative to the positive electrode (N/P ratio) was found to be a determining factor for cycle life and failure mode. At low N/P ratios (<2), pulverization is severe, and at high N/P ratios (>5), diffusional trapping dominates. As a result, optimal cycle life occurred at intermediate N/P ratios (3–4). However, this study utilized a 50% depth of discharge (DOD), which is useful as a diagnostic tool, but not practical for energy density purposes.

Alloying Al to form binary alloys has shown promise in extending cycle life, particularly with Si and Mg, both of which are abundant.[32–35] Alloying with 1 wt% Si and 5–10 wt% Mg has been shown to improve the cycle life and structural stability under practical conditions.[36,37] However, these studies used higher N/P ratios (>4), and the interactions between the modes of failure at various N/P ratios remain unexplored. It has been shown through cross-sections that these Al alloy anodes maintain an unreacted "current collector region" through cycling. It is hypothesized that, unlike 4N Al, the mode of degradation will not vary with the N/P ratio for Al alloys and form an unreacted region that enhances structural stability. It is expected that the structural stability observed at higher N/P ratios should be maintained at lower N/P ratios. Adopting a lower N/P ratio is preferable because it leads to an increase in energy density. Recent work has shown that pulverization and lithium trapping are inversely related in high-purity and alloyed Al foil anodes.[38] Identifying the dominant mode of degradation for each alloy is crucial for fully elucidating the effect of N/P. The FCE has been shown to vary with different Al alloys; therefore, it is hypothesized that the alloying element will influence the dominant mode of failure.

Overall, more mechanistic investigations are needed to uncover the relationship between the N/P ratios, composition, and failure mode. In this work, process–structure–performance relationships are developed for aluminum foil anodes alloyed with 1 wt% of silicon (Al–1Si), copper (Al–1Cu), and magnesium (Al–1Mg). After characterizing the anode materials, the foil thickness is varied to quantify the effects of the N/P ratio on the cycle life. The main mode of degradation is further explored by analyzing the electrochemical response (*e.g.*, nucleation overpotential and full cell polarization) for each alloy at different N/P ratios. We proceed to validate these observations through cross-sectional backscatter electron (BSE) imaging. Additionally, the reversible capacity is examined with a constant potential hold. Finally, the resistance through cycling is assessed with electrochemical impedance spectroscopy (EIS). We find that the dominant failure mode and performance are largely dictated by composition and N/P ratio.

Experimental

Material preparation

Three different aluminum foils were prepared by alloying 99.99% high purity aluminum (4N Al) with 1 wt% silicon, copper, or magnesium. The silicon and copper alloys were made by melting Al shot (Thermo Fisher, 99.99% purity) and the alloying element in a high purity graphite crucible with a top loading furnace at 760 °C. The melt was cast to form an ingot of approximately 40 mm × 30 mm × 10 mm. The magnesium alloy was cast with a 50/50 magnesium aluminum master alloy (Belmont Metals) and Al shot. All ingots were homogenized at 575 °C for 48 h, followed by slow cooling to room temperature. The top and bottom faces were then surfaced with a 1/2″ end mill to obtain a uniform thickness of ~7 mm. The ingots were then rolled down with an electric rolling mill (Durston, TUI 130) to approximately 1.2 mm for long term storage. Two inch sections were then cut from the storage ingot, a solid solution heat treatment was applied at 500 °C for 2 h, and then quenched in water. Aged ingots were heated at a set temperature for a set amount of time and then slow cooled to room temperature at a rate of 1 °C per minute after solutioning. Al–1Mg was aged at 90 °C for 96 h, Al–1Si was aged at 250 °C for 48 h, and Al–1Cu was aged at 200 °C for 96 h.

$LiFePO_4$ (LFP) cathode material was synthesized in-house.[39] The LFP electrodes were 94 wt% active material, 3 wt% carbon black (Imerys, Super C45), and 3 wt% poly(vinylidene fluoride) binder (Arkema, HSV-1810). The components were mixed into a slurry with *N*-methyl pyrrolidone (NMP), aiming for a solid loading of ~48 wt%, with a planetary centrifugal mixer (Thinky, Ar-100). The slurry was cast with a fixed blade to produce an areal capacity of 1.9–2.1 mAh cm^{-2}. The slurry was coated onto a double sided carbon coated Al current collector and then dried in a convection oven for 30 minutes at 110 °C. The electrodes were then calendared between two stainless steel shims in a heated roller at 110 °C to a density of 2.4 g cm^{-3} and dried overnight under vacuum at 130 °C. The electrolyte used for all experiments was LP57 (1 M $LiFP_6$ in 3 : 7 w/w ethylene carbonate (EC) : ethyl methyl carbonate (EMC)) with a 3 wt% fluoroethylene carbonate (FEC) additive. All electrolyte materials were obtained from Gotion and used as received.

Cell assembly

Electrochemical characterization was conducted with 2032 coin cells. Cells were constructed with two stainless steel (SS) spacers (5/8″ × 1 mm), two Celgard 2325 separators (3/4″ × 25 μm), and an SS conical spring. Full cells used an Al foil anode (9/16″ diameter) and an LFP cathode (1/2″ diameter). Half cells contained a Li metal chip (MTI, 5/8″ × 0.5 mm) and an Al foil electrode (7/16″ diameter). Half cells used nickel foam to seal the coin cell instead of a conical spring. The Li metal was cleaned with dimethyl carbonate (DMC) immediately before use. The thickness of the Al foil electrode was varied based on the N/P ratio. An electrolyte volume of 80 μL was used for all coin cells, and the cells were rested for 12 h after assembly to allow for proper electrolyte wetting.

Electrochemical characterization

Cycle life testing was conducted at room temperature with an Arbin battery cycler. All cells were initially formed with a constant voltage hold at 3.425 V (full cells) or 0.01 V (half cells) until a capacity of 0.3 mAh cm^{-2} was reached and then cycled galvanostatically at a C/10 (0.2 mA cm^{-2}) rate for the first three cycles. Subsequent cycling was done at a C/3 (0.667 mA cm^{-2}) rate with a voltage cutoff range of 2.5–3.5 V. The nucleation current response measurements were done with a Biologic VMP3 potentiostat by applying 3.425 V *vs.* a reference (ref) until a capacity of 0.3 mAh cm^{-2} was reached. Galvanostatic electrochemical impedance spectroscopy (GEIS) was carried out with a potentiostat on full cells at room temperature (~23 °C) for discharge on the first cycle. The full cells were all charged to 1.9 mAh cm^{-2} and discharged at a C/20 (0.095 mA cm^{-2}) rate. The following measurement conditions were used: applied current of −0.121 mA, 200 kHz–10 mHz, 10 points per decade, 121 μA amplitude, 0.1 period before each frequency, 1 measurement per frequency, and drift correction enabled. Electrochemical impedance spectroscopy (EIS) was performed at room temperature (~23 °C) in a charged state. The following measurement conditions were used for potentiostatic EIS: 0 V *vs.* open-circuit voltage (E_{oc}), 500 kHz–100 mHz, 10 mV perturbation amplitude, 10 points per decade, 0.1 period between each frequency, 1 measurement per frequency, and drift correction enabled.

Material characterization

X-ray diffraction (XRD) was conducted on 50 μm foils that were mounted on a glass sample holder with double-sided tape at a scan rate of 1.25° per min over a range of 2θ = 20–80° with a Rigaku Miniflex 600 diffractometer. For postmortem XRD, Kapton tape was used to seal the air-sensitive samples. Scanning electron microscopy (SEM) was coupled with energy dispersive X-ray spectroscopy (EDX) to observe the distribution of the alloying elements in the Al foil. Cycled cells were disassembled inside an argon filled glovebox and the foil anodes were rinsed with DMC. For cross-section images, electrodes were cut in half with a razor blade, then mounted on a silicon wafer, and milled with a Hitachi IM4000C broad beam ion mill. Milling was conducted inside an argon filled glovebox under the following conditions: 5 kV accelerating voltage and 1.25 kV discharge voltage. This allows for ~1 min per μm mill time. Any cycled electrodes too brittle for ion milling were obtained *via* small flakes from the disassembled cell. These flakes were mounted on the SEM stub and immediately taken to be imaged. SEM images were recorded on a TESCAN VEGA3 with an acceleration voltage of 15 kV, a beam intensity of 14, and a BSE detector. Surface images were acquired at a working distance of ~15.50 mm, and cross-section images were acquired at a working distance of 12 mm. To calculate the LiAl island size, a linear intercept method was used in the horizontal and vertical directions. Each image had ten lines drawn across the image. Every island boundary that crossed the drawn line was counted, and the total length of the line was divided by the intercept, yielding an average island size.

Results and discussion

Material characterization

Studies have demonstrated that the cycling performance of Al foils can be improved by including small amounts (<2 wt%) of alloying elements.[40,41] Li *et al.* varied the Si content from 0–4 wt% and found that 1 wt% exhibited the greatest improvement in cycle life and structural stability.[36] Therefore, 4N Al was alloyed with 1 wt% of silicon, magnesium, or copper, designated as Al–1X (X = Si, Mg, Cu). These elements are known to form a solid solution with Al.[42–44] To verify that each alloy remained in a solid solution condition, XRD and EDX mapping were conducted on cold-rolled foils prepared from ingots that underwent a solid solution heat treatment. XRD scans of Al–1Cu and Al–1Mg show the foils are solid solutions, and Al–1Si exhibits a peak around $2\theta = 28°$, indicating that the Si phase is present (Fig. 1a–c). EDX mapping reveals that Al–1Si forms Si agglomerations, while Al–1Mg and Al–1Cu remain as solid solutions following cold rolling (Fig. 1d–f). An aging heat treatment was applied to the ingot before cold rolling to compare with the solid solution heat treatment. The XRD and EDX mapping of the cold-rolled foils show a similar distribution between both heat treatments (Fig. 1a–c and g–i). The Si agglomeration size (median 4 and 4.6 μm) and distribution also remain similar between the solution-treated and aged Al–1Si seen in Fig. S1.

The cycle life of the cold-rolled foils from the solution-treated and aged ingots was compared. The solution-treated Al–1Si exhibits better cycling stability at a low capacity (Fig. 1j). In contrast, aged Al–1Si has a higher FCE (66% *vs.* 53%) and cycles at a higher capacity, though it experiences a steady decline in capacity retention. The Al–1Cu solution-treated and aged alloy presents identical cycling behavior (Fig. 1k). It is possible that increasing the Cu content in Al–1Cu would cause copper to precipitate out of solid solution with heat treatments. Then, it may cycle similarly to the aged Al–1Si. Interestingly, the effect of the aging treatment on Al–1Mg is inverse to that observed with Al–1Si. Both the solution-treated and aged Al–1Mg remain in solid solution and cycle at a similar capacity. Although the aged Al–1Mg improves cycling stability, it stabilizes at a lower capacity than the solution-treated alloy (Fig. 1l). Analogous aluminum alloys can provide insights into the alloy response to heat treatment. The 2XXX (Al–Cu) and 4XXX (Al–Si) series are strengthened by heat treatments.[45] In contrast, the 5XXX (Al–Mg) series is strengthened through strain hardening. Overall, the heat treatable alloys (Al–1Si and Al–1Cu) have a lower FCE and improved long-term stability, compared to the strain hardenable Al–1Mg, which has improved capacity retention at the expense of cycle life. Foils cold-rolled from the aged ingots were used for the remainder of this work.

Previous studies have demonstrated that increasing the grain boundary density in the foil improves lithiation kinetics, facilitating uniform LiAl nucleation.[27,30] Heat treatments have been used as a strategy to adjust the grain boundary density and internal stresses to improve the structural integrity over cycling.[28,46,47] The hardness of the foil has also been shown to be

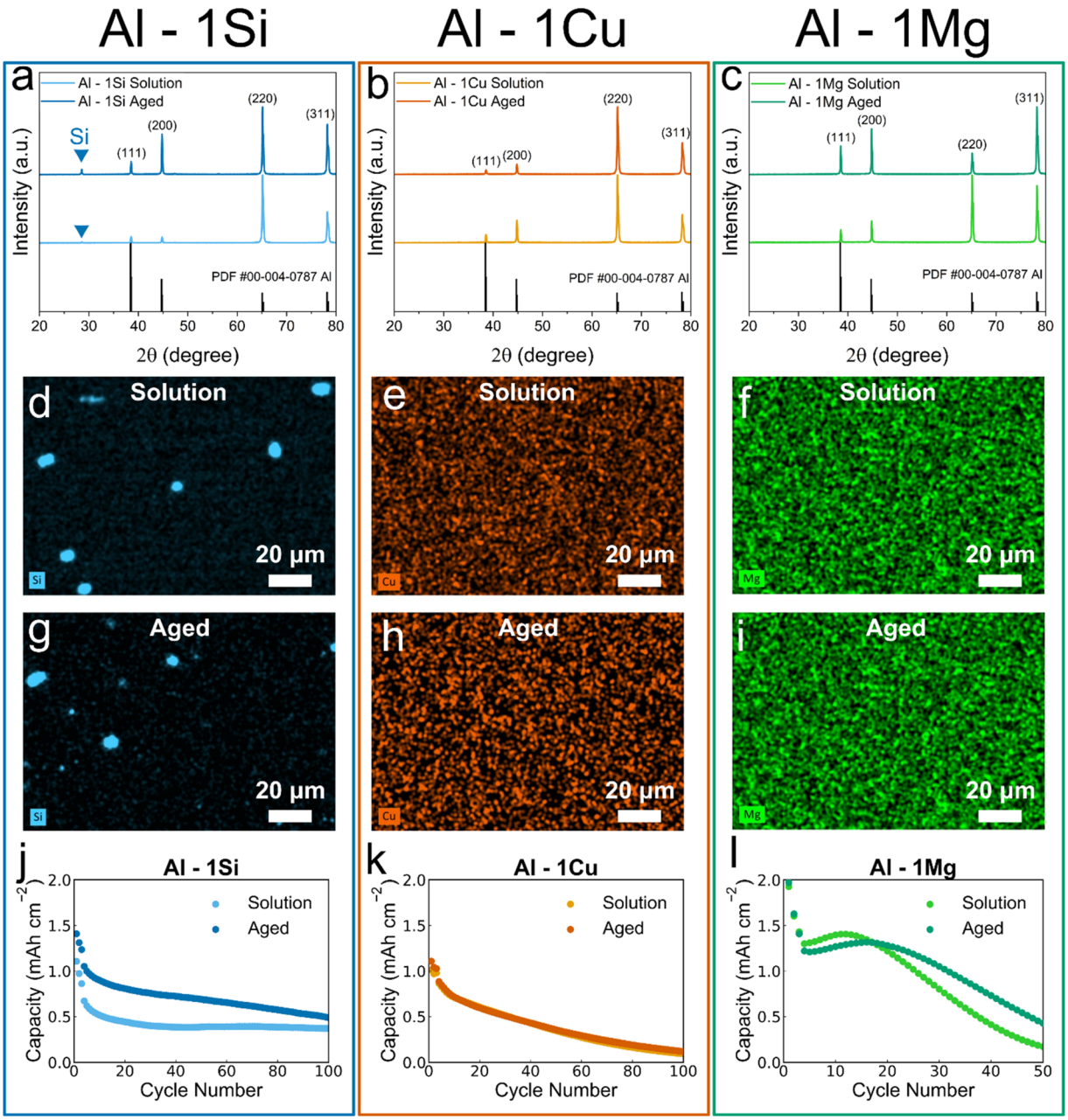

Fig. 1 Comparison of a cold rolled foil from a solution-treated and aged ingot. (a–c) XRD pattern for Al alloyed with (a) silicon, (b) copper, and (c) magnesium, compared to the powder XRD standard for Al. (d–i) EDX mapping for Al foils alloyed with (d and g) Si, (e and h) Cu, and (f and i) Mg. (j–l) Cycle life test of LFP||Al full cells at a C/3 rate to compare the solution-treated and aged Al alloyed with (j) Si, (k) Cu, and (l) Mg.

a major contributing factor to uniformity of lithiation, mechanical resilience, and improved cycling performance.[25,26] Hardness values ranging from 54 to 109 HV for various alloys have been attributed to improved performance.[25,27,37] It is likely that aging the ingot before cold rolling allowed for improved balance between grain boundaries, residual stresses, and hardness, resulting in a foil with improved structural integrity. Future work should comparatively assess how heat treatments affect these properties in ingots and foils.

N/P ratio optimization for cycle life

Despite the low alloying addition of 1 wt%, to ensure accurate N/P ratio calculations, the capacity of the alloy foils is compared with that of 4N Al. At the anode, Cu is considered an inactive element, while Mg and Si are active materials that electrochemically react with lithium.[4,5,48] Half cells of the Al alloy foils were charged to 0 V *vs.* Li/Li^+, and the measured capacities were compared to that of a 4N Al foil shown in Fig. S2. All the Al alloy and 4N Al foils had a similar measured capacity (~1080 mAh g^{-1}) that is higher than the theoretical capacity (993 mAh g^{-1}). Zheng *et al.* recently found that Al foils hold more lithium than

Table 1 N/P ratio and the corresponding foil thickness required for a 2 mAh cm^{-2} LFP cathode

N/P ratio	Foil thickness (μm)
1	7
2	14
3	21
4	28
7	49

the ideal stoichiometry, resulting in a capacity higher than the theoretical.[49] Furthermore, the lithiation potential for all the alloys is consistent with that of 4N Al, with no other plateaus emerging. Therefore, it is suitable to use the theoretical capacity of 4N Al for N/P ratio calculations for the alloy foils.

To investigate the effect of the N/P ratio on the performance of the Al alloy foils, cycle life testing was performed by pairing a 2 mAh cm^{-2} LFP cathode with various Al alloy foil thicknesses (Table 1). For the Al–1Si foils, there are two distinct types of cycling behavior (Fig. 2a). Initially, all Al–1Si foils lose large amounts of capacity (>4%) for the first 5 cycles, except for a N/P ratio of 1 (Fig. S3a). As the foils continue to cycle, foils with an N/P of 4 and 7 continuously lose a small amount (<1%) of capacity every cycle, and the coulombic efficiency (CE) stabilizes at ~98–99% by cycle 5 (Fig. S3d). The foils with an N/P of 2 and 3 lose ~1–2% of the capacity until they reach about 10 cycles, where they then begin to gain approximately 1% capacity every cycle. This leads to a CE greater than 100%. An N/P of 1 has a 4% capacity gain and then is followed by a large amount of capacity loss every cycle. Improved cycling appears to be with an N/P of 2–3, which cycles at a higher capacity.

Similarly, Al–1Cu also experiences two types of cycling behaviors (Fig. 2b). An N/P greater than 2 shows a large initial loss of capacity in the first 5 cycles (>2%), but then begins to experience less than 1% loss each cycle (Fig. S3b). This is reflected in the CE of ~98–99% (Fig. S3e). Foils with N/P ratios of 1 and 2 gain up to 8% capacity, but subsequently exhibit continuous capacity loss of 2–5% every cycle. Our previous work has shown that a gradual loss of capacity is an indicator of diffusional trapping in 4N Al.[31] This behavior and the low FCE suggest that both Al–1Si and Al–1Cu are diffusional trapping dominated. The lower N/P ratios (1–3) likely gain capacity during cycling due to fracturing that allows trapped lithium to become accessible. However, Al–1Cu may be affected by pulverization to a greater extent compared to Al–1Si due to the increased capacity fade for all N/P ratios.

Alternatively, Al–1Mg foils appear to exhibit one type of cycling behavior that converges beginning at an N/P of 4 (Fig. 2c). As the N/P ratio increases, the number of cycles until 1 mAh cm^{-2} capacity is reached (50% state of health) increases (Fig. S4). However, the capacity for the plateau-like region seen in the cycle life testing decreases from about 1.8 to 1.2 mAh cm^{-2} as the N/P is increased. There is an apparent tradeoff between capacity retention and cycle life. In 4N Al foils, large amounts of capacity loss suggest pulverization as the main failure mechanism.[31] Therefore, it is likely that Al–1Mg is dominated by pulverization behavior, as it also has a relatively high FCE and continually loses large amounts of capacity (>5%) in the first 10 cycles (Fig. S3c). However, the higher N/P ratios may still be affected by diffusional trapping. The CE further supports pulverization dominated degradation as it does not stabilize across the N/P ratios (Fig. S3f). Continuous capacity loss is further amplified by SEI growth, especially at lower N/P ratios, where pulverization is greatest.

The presence of the nucleation overpotential on charge can be attributed to a surface passivated with α-Al that requires LiAl nucleation on the subsequent cycle.[50] It can be expected that when LiAl is present in the structure, the nucleation barrier is lessened or eliminated.[51] Repeated nucleation during cycling has been linked to accelerated pulverization of the structure.[30] Given that two of the Al alloy foils show two distinct cycling behaviors observed across the N/P ratios in the cycle life, the overpotentials of foils with N/P ratios of 2 (thin) and 7 (thick) are compared. The nucleation overpotential for an Al–1Si foil with an N/P ratio of 2 decreases through cycling and grows after capacity fade begins (Fig. 3a). The decrease in the overpotential is likely caused by increased access to the trapped LiAl. Al–1Si with an N/P ratio of 7 maintains a stable overpotential that is initially lower than the other alloy foils with a N/P ratio of 7 (Fig. 3b). The N/P ratio of 7 may maintain a larger "current collector" region that stabilizes the structure, whereas the N/P ratio of 2 is subject to reduced mechanical support, enabling the contraction/expansion to induce more fracturing and access to trapped LiAl. Both Al–1Cu foils with N/P ratios of 2 and 7 are similar to the Al–1Si foil with an N/P ratio of 2 (Fig. 3c and d). It

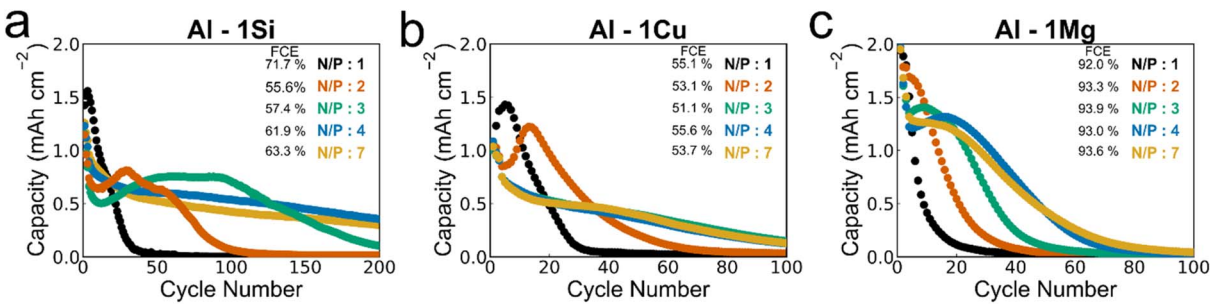

Fig. 2 Cycle life data for N/P ratio optimization. Cycle life test for an LFP full cell with an areal capacity of 2 mAh cm^{-2} at a C/3 rate, while varying the anode foil thicknesses to achieve different N/P ratios of (a) Al–1Si, (b) Al–1Cu, and (c) Al–1Mg.

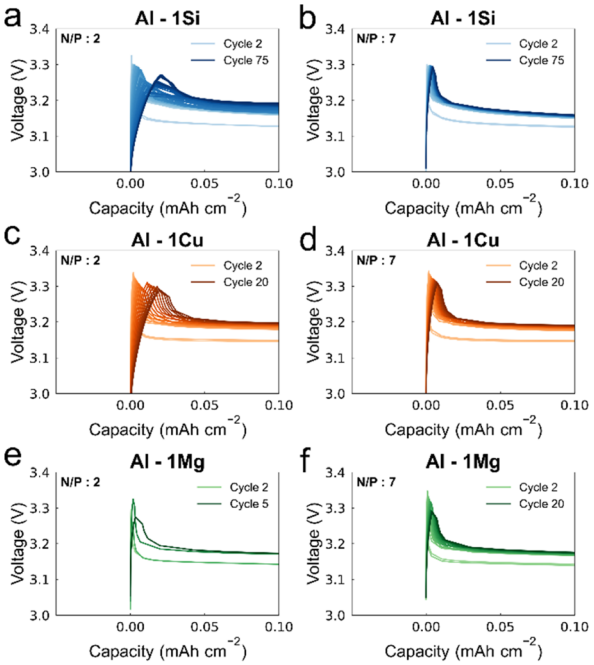

Fig. 3 Nucleation overpotential during cycling. Voltage *vs.* capacity plots highlighting the overpotential during charge for (a and b) Al–1Si, (c and d) Al–1Cu, and (e and f) Al–1Mg foils with an N/P ratio of (a, c and e) 2 and (b, d and f) 7.

can be expected that Al–1Cu experiences increased fracturing compared to Al–1Si. Al–1Cu with an N/P ratio of 2 shows an increase in the overpotential at an earlier cycle than Al–1Si (cycle 13 *vs.* 57). This is when capacity begins to fade after the capacity gain.

Al–1Mg with an N/P ratio of 2, hypothesized to be pulverization dominated, presents nucleation overpotential growth until cycle 5 when capacity begins to fade (Fig. 3e). In contrast, Al–1Mg with an N/P ratio of 7 initially exhibits a large overpotential that decreases through cycling. This behavior is likely influenced by a combination of diffusional trapping and pulverization at a high N/P ratio (Fig. 3f). Across all Al alloys, fracturing at lower N/P ratios increases the ability to remove LiAl from the foil, effectively transforming back to α-Al, which requires nucleation in the following cycle. However, at higher N/P ratios, a continued decrease in the overpotential is attributed to the gradual access to trapped LiAl. Overall, diffusional trapping leads to lower nucleation overpotentials, while pulverization leads to higher and increasing overpotentials. Future work should focus on surveying Al alloys at lower N/P ratios that eliminate or mitigate repeated nucleation to improve structural stability.

Analysis of the voltage profile provides insight into the processes occurring during degradation, presented in Fig. S5. A sloping voltage drop during discharge can be attributed to diffusional kinetic limitations.[31,52] The Al–1Si foils exhibit a sloping voltage tail that becomes more apparent at higher N/P ratios. This suggests that Al–1Si experiences diffusional trapping regardless of the N/P ratio. Al–1Cu foils with an N/P ratio of 2 encounter hindered Li^+ transport before cycle 13, reflected in the sloping voltage tail. After the maximum capacity has been gained and fade begins, a sharp voltage drop during discharge occurs. This is likely due to the structure becoming increasingly fractured every cycle, suggesting that Al–1Cu experiences a mixed mode. However, the N/P ratio of 7 is primarily dominated by diffusional limitations, similar to Al–1Si. For both Al–1Mg foils with an N/P ratio of 2 and 7, a consistent sharp voltage drop occurs. Interestingly, the N/P ratio of 7 exhibits a kink in the discharge voltage at cycle 20, shifting to lower voltages through cycling. It is possible that more of the surface is pulverized through cycling, accessing more of the trapped LiAl (Fig. S6). Although fracturing can improve the kinetics and accessible capacity, excessive pulverization degrades structural integrity and increases SEI formation.[53] Such behaviors are reflected in the full cell polarization. Overall, an N/P ratio of 7 exhibits kinetic limitations for all alloys, while the kinetic behavior is alloy dependent for foils with an N/P ratio of 2.

The full cell polarization growth was calculated through cycle 50 by calculating the difference between the charge/discharge voltages labeled as ΔV in Fig. S5. The growth in polarization can be linked to structural degradation and SEI growth.[54–56] LFP half-cell data present no growth through cycling, ensuring that polarization growth is minimally influenced by the cathode (Fig. S7). Al–1Si and Al–1Cu exhibit, respectively, increases in polarization of 42 mV and 72 mV for an N/P ratio of 2, while remaining constant for an N/P ratio of 7 (Fig. 4a, b and d). Li *et al.* have shown that Al–1Si can impede porosification, while maintaining the mud cracking structure for up to 30 cycles.[36] Mud cracking has a similar structure to dried mud, which enhances the reversible expansion/contraction, while preventing additional cracking.[57] The mud cracking and any minor cracking enable capacity recovery, while maintaining structural stability, leading to less SEI and polarization growth. The overall higher polarization for Al–1Cu could be governed by the mixed diffusional trapping and

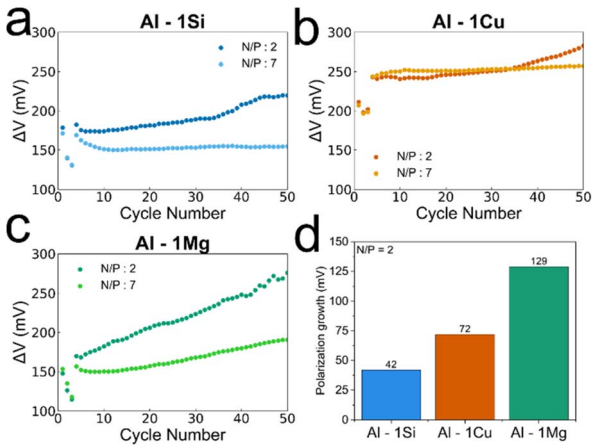

Fig. 4 Full cell polarization growth. Comparison of the full cell polarization for foils with N/P ratios of 2 and 7 in (a) Al–1Si, (b) Al–1Cu, and (c) Al–1Mg foils paired with an LFP cathode. (d) Comparison of the increase in polarization from cycle 1 to 50 cycles across the Al alloy foils with an N/P ratio of 2.

pulverization effects believed to occur. Moreover, the polarization of Al–1Mg foil with an N/P ratio of 2, which is believed to be pulverization dominated, continually increases to approximately 129 mV (Fig. 4c and d). Although the Al–1Mg foil with an N/P ratio of 7 encounters diffusional trapping, it also sustains severe pulverization on the surface, causing increased polarization through cycling. The polarization growth seen in pulverization dominated failure is likely caused by irreversible capacity loss due to SEI growth and loss of electrical contact. Overall, the mechanical degradation of the structure is correlated with an increase in the full cell polarization.

Investigation of degradation mechanisms

Cold rolling a foil alters the microstructure of the pristine foil (before lithiation) and may impact performance. Since the LFP cathode is kept constant, the N/P ratio is achieved through different foil thicknesses. The N/P ratio essentially serves as a measure of the degree of cold rolling. In 4N Al foils, potentiostatic formation largely mitigates any difference in the microstructure caused by cold rolling at various N/P ratios.[31] This behavior is expected to be observed in Al–1X foils across all N/P ratios, with each alloy producing a distinct LiAl island size. The EDX mapping shows that the alloying element distribution, including the Si agglomeration size, remains consistent for all N/P ratios (Fig. S8).

To compare the effect of cold rolling on the LiAl formation, nucleation with potentiostatic formation (3.425 V) was performed until a capacity of 0.3 mAh cm^{-2} was reached on a foil with N/P ratios of 2 and 7 for each alloy. The current response was recorded, and the resulting LiAl island sizes were measured. Analysis of the current response allows evaluation of the nucleation behavior of LiAl.[58] Generally, a higher magnitude correlates to a faster reaction rate and smaller LiAl islands. The corresponding current response, surface SEM images, and measurements of the LiAl islands are taken for each alloy. The current response for both Al–1Si foils with N/P ratios of 2 and 7 plateaus around 4–5 mA cm^{-2} and reaches the capacity limit in ~5 minutes (Fig. S9). Based on the surface SEM images, both foils have full LiAl coverage with a median island size of 1.7 μm. Al–1Cu produced an identical current response for both N/P ratios (plateau at 3 mA cm^{-2}) that reached the capacity limit in 7 minutes for N/P ratios of 7 and 8 minutes for an N/P ratio of 2 (Fig. S10). Both foils similarly formed larger LiAl islands with the median island size ranging from 3.6 to 4.3 μm, with increased heterogeneity and small regions of unreacted foil shown in Fig. S11.

The Al–1Mg foil current response for the N/P ratio of 7 is higher (plateau at 5 *vs.* 3 mA cm^{-2}) and reaches the capacity limit 2 minutes earlier than the foil with a N/P ratio of 2 (Fig. S12). The median LiAl island size is 2.5 μm for both foils; however, the N/P ratio of 2 exhibits a subset of larger islands reaching 3.5 μm. Any differences between the N/P ratios may be attributed to the hardness, which is affected by the degree of cold rolling.[59,60] Since the islands between both N/P ratios are similarly sized, further lithiation will transform the islands into a columnar structure of comparable dimensions. Overall, potentiostatic formation minimizes the effect of the pristine foil microstructure created during cold rolling on the LiAl formation. Future work should focus on understanding the effect of hardness on LiAl island size for Al alloy foils.

To evaluate the structural evolution, cross-section BSE images were taken of the alloy foils with N/P ratios of 2 (15 μm) and 7 (52 μm) after the first and fifth discharge (delithiated state). A color overlay for the cross-sectional and surface images is displayed in Fig. S13 and S14. Potentiostatic formation was performed to ensure that a uniform LiAl columnar structure was formed.[29–31] In the first cycle, the Al–1Si foil with an N/P ratio of 2 reveals a LiAl columnar structure that has grown through the foil with minimal fracturing between the columns, indicating signs of diffusional trapping (Fig. 5a). The "mud-cracking" morphology, commonly associated with silicon, is seen on the surface.[40,57] As the foil is cycled, the structural integrity is retained with ~40% volume expansion, while maintaining an unreacted region on the bottom (Fig. 5b). However, this "current collector" region offers minimal structural stability, as evidenced by the deformation seen on the backside of the foil after the first discharge (Fig. S15). Similarly, the thick foil maintains minimal fracturing between columns, but is subjected to increased diffusional trapping effects and a ~17% volume expansion (Fig. 5c and d). The fracturing seen on the surface may be attributed to any non-uniform growth of the SEI, which may induce localized current concentration and micro-scale pulverization (Fig. S14d). Even when diffusional trapping aids in maintaining the columnar structure, fracturing is still observed.

The Al–1Cu foil with an N/P ratio of 2 is largely indistinguishable from the Al–1Si foil with a N/P of 2, due to the columnar formation and mud cracking; however, there is increased fracturing between the columns seen on the surface (Fig. 5e). By cycle 5, cracking has increased and propagated through the foil, inducing a 67% increase in the foil thickness (Fig. 5f). It has been shown that cracking/fracturing allows trapped LiAl to become accessible during cycling.[21,38] The early onset and severity of cracking correlate to the larger gain in capacity seen around cycle 10, unlike Al–1Si, which exhibits smaller amounts of capacity gain at later cycles. In fact, as Al–1Cu is further cycled, the structure is increasingly pulverized and transformed into a porous material (Fig. S16). The Al–1Cu foil with an N/P ratio of 7 maintains the columnar structure with diffusional trapping effects present and a ~25% volume expansion (Fig. 5g and h). The surface passivation and cracking have increased compared to the Al–1Si foil with an N/P of 7.

The Al–1Mg alloy presents a different structural transformation. After the first discharge, the columnar structure in the foil with an N/P ratio of 2 undergoes uniaxial contraction, leading to structural collapse and minimal signs of diffusional trapping (Fig. 5i). By the fifth cycle, the foil thickness has expanded 86%, and the foil is completely pulverized into a porous structure (Fig. 5j). Repeated fracture creates a porous structure that leads to large volume expansion in foils.[61] The surface images indicate that mechanical pulverization was accelerated around cracks, which is favorable for nucleation.[62] When the N/P ratio is 7, surface images show minor cracking

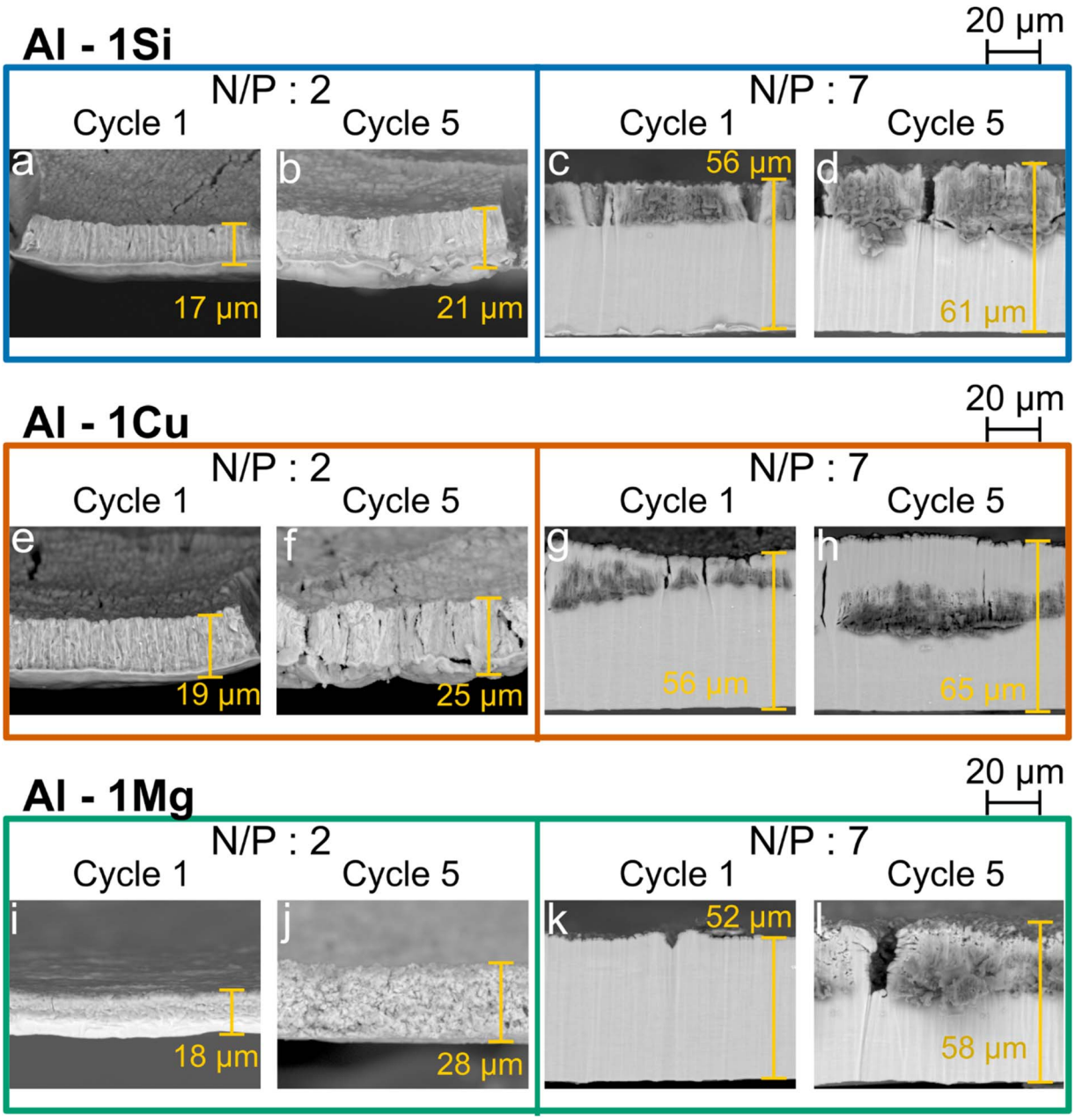

Fig. 5 Effect of the alloying element and N/P ratio on the structural evolution. BSE cross-section images of the morphological evolution of the (a–d) Al–1Si, (e–h) Al–1Cu, and (i–l) Al–1Mg foil anodes. The panels compare foils with N/P ratios of (a, b, e, f, i and j) 2 and (c, d, g, h, k and l) 7. Images were acquired on discharge at cycles (a, c, e, g, i and k) 1 and (b, d, f, h, j and l) 5.

between the columns, but exhibit an increase in large-scale cracks after the first cycle. Unlike Al–1Si and Al–1Cu, there is no trapped LiAl in the cross section, which is reflected by the high FCE (93%) (Fig. 5k). The combination of a high FCE and the reinforced structural stability from the unreacted "current collector" enables the foil to return to its original thickness. However, by the fifth cycle, diffusional trapping becomes evident (Fig. 5l). Interestingly, unlike the other thick foils, Al–1Mg exhibits a lower expansion of ~12% and faces severe pulverization on the surface. The trapped LiAl limits the overall columnar contraction, unlike when the N/P is 2. Cracking is then localized to the surface rather than propagating through the entire foil. The increase in access to the trapped LiAl allows further contraction and reduces volume expansion. Overall, the cross-sectional images provide initial insights into the main mode of degradation for each alloy foil with different N/P ratios.

To probe the amount of capacity trapped in the bulk, a constant voltage was applied until a C/1000 current was reached at the end of the fifth discharge. Applying a constant voltage allows sufficient time for any reversible lithium trapped to diffuse through the foil.[63] There is a clear trend among the different alloy foils with an N/P ratio of 2. The more pronounced

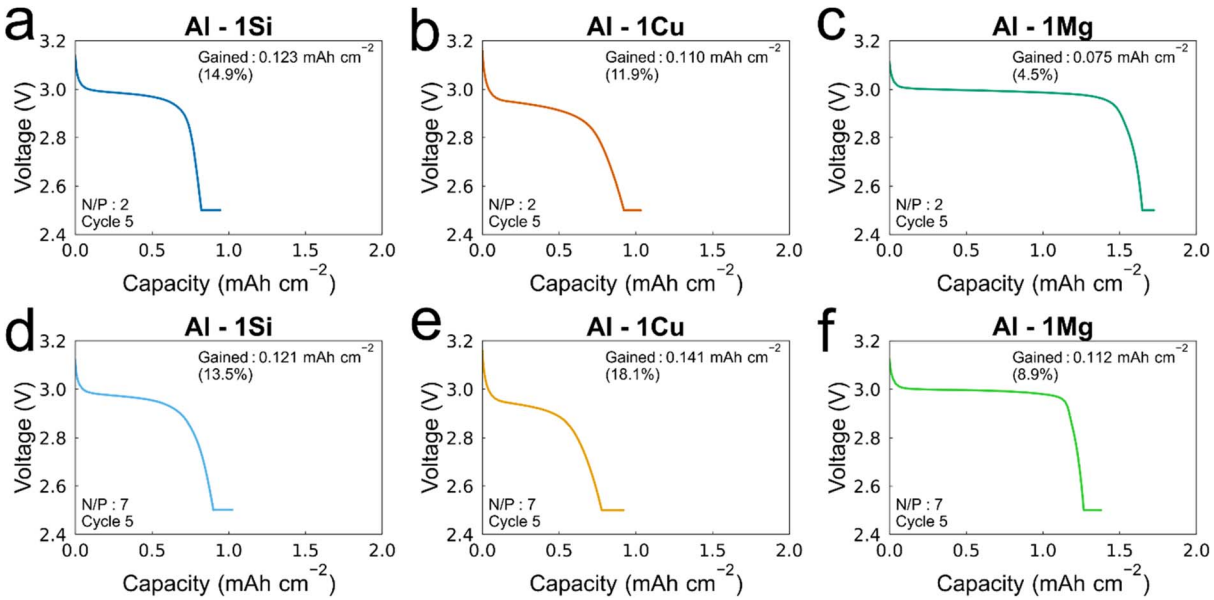

Fig. 6 Voltage hold after the fifth discharge to probe reversible capacity. Voltage *vs.* capacity plots of the 5th discharge with a voltage hold for foils with an N/P ratio of 2 for foils alloyed with (a) Si, (b) Cu, and (c) Mg and an N/P ratio of 7 for foils alloyed with (d) Si, (e) Cu, and (f) Mg.

the mechanical degradation of the structure, the less capacity is gained after the voltage hold (Fig. 6a–c). The time to reach the current cutoff also decreases as pulverization increases (Fig. S17). The Al–1Si foil, which is diffusional trapping dominated, required a longer voltage hold duration (1.6 h) to reach the current limit, compared to Al–1Mg (0.7 h), which is pulverization dominated. During the voltage hold, the columnar structure continues to contract, increasing cracking and allowing access to trapped LiAl. This increased capacity recovery is reflected in the charge capacity on cycle 6 (Fig. S18). Al–1Si and Al–1Cu recover more capacity compared to Al–1Mg. Comparing the nucleation overpotential on the following charge for both discharge conditions further supports the distinction between degradation modes (Fig. S19). All the alloys exhibit an increase in the overpotential after the voltage hold, consistent with greater surface passivation due to increased Li extraction.

For an N/P ratio of 7, all the Al alloy foils generally extracted more capacity and required a longer voltage hold duration (2–2.7 h) than the foils with a N/P ratio of 2 (Fig. 6d–f). However, for Al–1Si, the N/P ratios of 2 and 7 obtain a similar capacity. The charge capacity on the following charge is higher than the

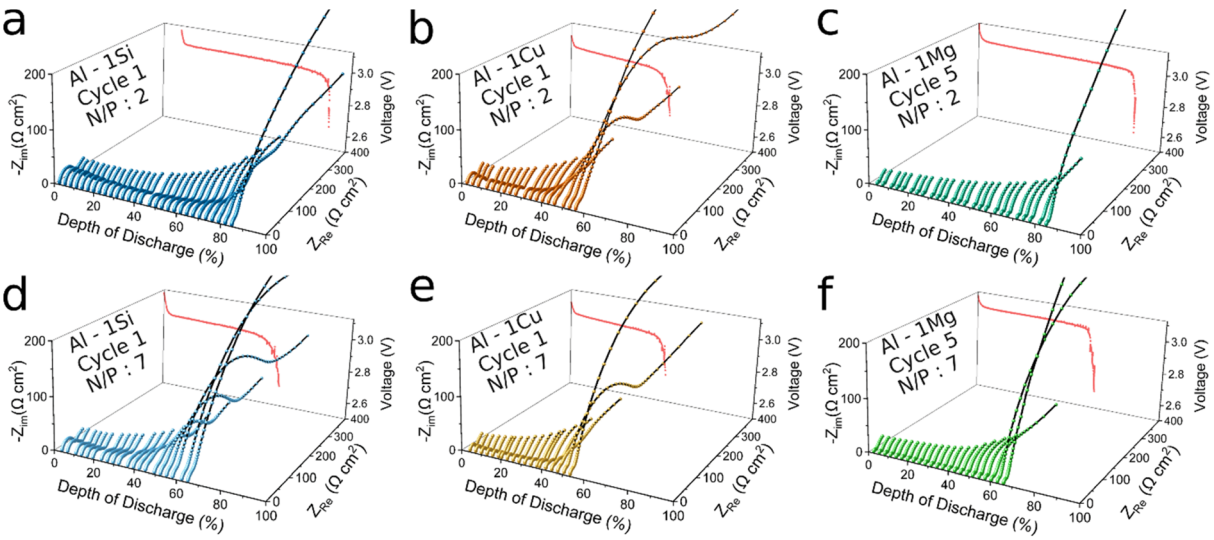

Fig. 7 *Operando* galvanostatic electrochemical impedance spectroscopy (GEIS) for diffusional behavior during discharge. Impedance spectra (200 kHz–10 mHz) and voltage *versus* depth of discharge collected during discharge at a C/20 rate for (a and d) Al–1Si, (b and e) Al–1Cu, and (c and f) Al–1Mg foils with an N/P ratio of (a–c) 2 and (d–f) 7.

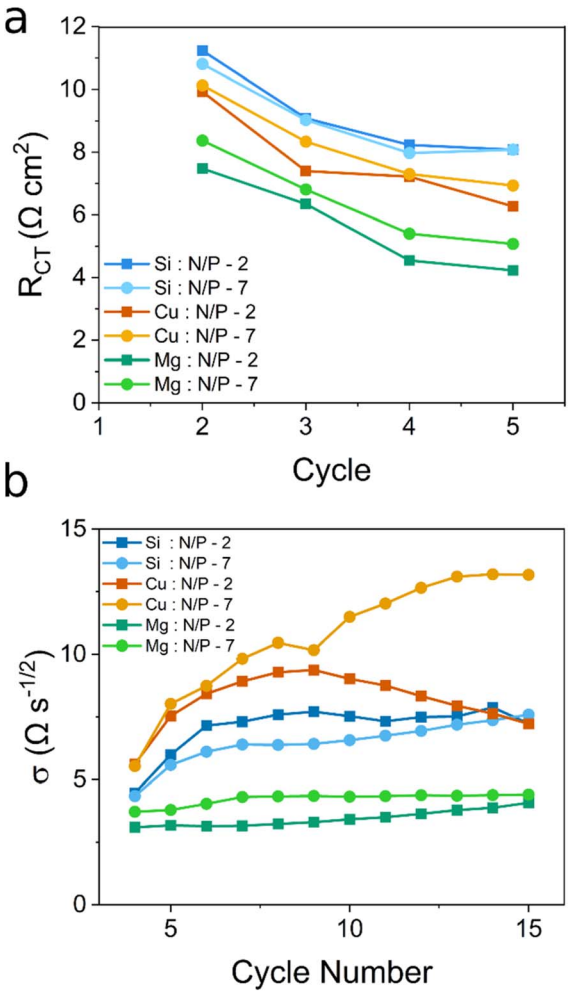

Fig. 8 Impedance evolution through cycling. Measured (a) charge-transfer resistance R_{ct} and (b) Warburg coefficient σ as a function of cycle number for each alloy anode at N/P ratios of 2 and 7.

standard discharge condition, but similar across alloys. During discharge, foils with an N/P ratio of 7 are subject to passivation under the standard voltage cutoff (Fig. 5). The structural reinforcement from the unreacted current collector region mitigates the extent of fracturing during the voltage hold, compared to the foils with an N/P ratio of 2. The nucleation overpotential on the subsequent charge is similar under both discharge conditions, supporting diffusional trapping as the dominant failure. Overall, for both N/P ratios, capacity recovered during the voltage hold is primarily from the trapped LiAl becoming accessible.

Considering that pulverization causes electronic isolation and SEI growth, pulverization dominated degradation would have less reversible capacity available, like Al–1Mg. Until the structure can be stabilized through cycling, a higher discharge capacity is achieved at the expense of structural integrity. Greater Li extraction exacerbates uniaxial contraction, leading to fracturing and eventually pulverization. Post-mortem XRD confirms complete delithiation in Al–1Mg with both N/P ratios after the first cycle (Fig. S20). By cycle 5, the LiAl phase is present but more prominent at a N/P of 7. This is consistent with greater diffusional trapping, as confirmed by the cross-sectional image and XRD of Al–1 Si and Al–1Cu after the first discharge (Fig. 5l). When the structure remains intact and LiAl remains in the bulk (*i.e.*, N/P = 7), gradual capacity recovery further supports diffusional trapping as the main mode of degradation for Al–1Si and Al–1Cu at high N/P ratios.

Galvanostatic electrochemical impedance spectroscopy (GEIS) during discharge was employed to characterize the diffusion behavior of the alloy foils. A rate of C/20 was used for the discharge. Progressive growth in the impedance spectra during discharge reflects the onset of diffusional limitations. On the first cycle, Al–1Si with an N/P of 2 discharges 84% of the capacity, while that with an N/P of 7 is able to discharge 65% (Fig. 7a and d). Both Al–1Cu foils discharge to ~55%, suggesting worse diffusional kinetics (Fig. 7b and e). In comparison, the Al–1Mg foils with both N/P ratios discharge to ~95% (Fig. S21). However, as Al–1Mg is cycled, the foil with a N/P of 7 experiences diffusional trapping behavior, reflected in the cycle life and further supported by GEIS at cycle 5. The foil with a N/P of 2 shows minimal impedance growth and discharges 82% of the capacity (Fig. 7c). The foil with a N/P of 7 exhibits increased impedance growth, similar to the diffusional trapping foils, and discharges 66% of the capacity (Fig. 7f). Overall, the foil with a N/P of 7 faces diffusional limitations regardless of alloying elements. However, at an N/P of 2, the alloying addition influences the diffusional behavior.

To further validate the dominant mode of degradation, EIS was collected through cycling to understand the evolution of lithium transport. A reduction in the charge-transfer resistance (R_{ct}) can be expected if the surface area is increased (pulverization).[64] The R_{ct} was measured for cycles 2 to 5 with the equivalent circuit in Fig. S22 and 8a. A summary of the fitted parameters is shown in Table S1. The first cycle is considered the formation cycle and was excluded. Overall, the alloy foil that exhibited the highest degree of pulverization in the cross-sectional images (Al–1Mg) yielded the lowest R_{ct}, while the alloy foil that remained structurally intact (Al–1Si) exhibited the highest. The R_{ct} for Al–1Cu produced intermediate values, consistent with the mixed modes displayed. Generally, a higher N/P ratio presents a higher R_{ct} than the lower N/P ratio, likely caused by the increased support of the unreacted layer that suppresses fracturing.

Additionally, a lengthening Warburg tail indicates a worsening diffusional limitation.[65] The Warburg coefficient was tracked to gain insights about diffusion through cycling (Fig. 8b). A larger Warburg coefficient corresponds to slower diffusion, whereas a smaller Warburg coefficient suggests faster diffusion.[66] Alloy foils, believed to be largely affected by diffusional trapping, exhibit a growing Warburg coefficient through cycling. Any decreases observed correlate to capacity gains during cycle life, which is caused by cracking. This can be correlated with the Warburg tail growth, presented in Fig. S23. When pulverization is the dominating mechanism, the Warburg coefficient is low or constant, as seen for Al–1Mg. The Warburg tail remains consistent and is shorter than that of the other alloys. Although Al–1 Mg with an N/P ratio of 7

experiences diffusional trapping limitations, the surface of the foil undergoes a high degree of pulverization. These findings are consistent with the GEIS data and highlight the severe diffusional limitations observed in Al–1Cu. Collectively, these findings reveal a clear trend linking increased pulverization to decreased impedance.

Future studies should avoid using high N/P ratios (>4) as they are not only detrimental to energy density but also induce diffusional trapping. It is important to note that studies should be done under lithium-limited conditions (full cells or lithium-limited inventory cycling) to understand the failure mechanisms in practical conditions.[65] Even with very thick Al foils, the continuous addition of lithium will eventually cause pulverization from the repeated expansion/contraction regardless of the alloy addition. Ideally, employing a lower N/P ratio (<4) is preferred to increase the energy density that outperforms graphite anodes. In 4N Al foil anodes, low N/P ratios led to pulverization dominated degradation, whereas an N/P ratio of 4 resulted in optimal cycle life with a balance between the two degradation modes. This work found that for alloys with diffusional trapping limitations, a lower N/P ratio of 2–3 provided improved cycle life. Alloys that experience pulverization dominated degradation maintain a higher capacity retention at the expense of long-term stability, with improved performance at an N/P ratio of 4. Similar to 4N Al, balancing the effects of both failure mechanisms improves performance. Future work could focus on developing strategies to tailor the influence of each mode of failure through composite foils, cladding, microstructural design through processing conditions (*e.g.*, roll speed or heat treatment) or multicomponent alloys.[24,67–70]

Conclusion

In this work, the microstructural evolution and mode of degradation of Al alloy foils were investigated as a function of cell design. First, we explored a cold-rolled foil from an ingot that underwent a solid solution heat treatment or aging treatment. Foils that were cold rolled from an aged ingot demonstrated improved cycle life. The N/P ratio was optimized and found to be a determining factor in cycling behavior and failure mode. For all Al alloy foils, a high N/P ratio led to diffusional trapping behavior and continuous capacity loss during cycling. By contrast, cycle life and the mode of degradation are dependent on the alloying element at low N/P ratios. Al–1Si foil anodes experienced diffusional trapping degradation, characterized by a low FCE, gain in capacity with improved long-term cycling, decrease in the nucleation overpotential, and gradual increase in the full cell polarization. Al–1Mg foil anodes exhibited pulverization dominated failure defined by a high FCE, higher capacity retention with a shorter cycle life, and a pronounced increase in both the nucleation overpotential and full cell polarization. The Al–1Cu foil anodes underwent a mixed mode and exhibited characteristics of both.

The dominant failure mode was further validated by microstructural evolution observations, reversible capacity testing, and impedance growth through cycling. Cross-sectional imaging revealed that for all alloys with an N/P ratio of 7, LiAl remained trapped in the foil. Alloys dominated by diffusional trapping maintained structural integrity, while pulverization dominated failure led to a porous structure. The more an alloy foil experiences pulverization, the less capacity recovered with a constant voltage hold. Increasing pulverization also leads to a decrease in the impedance. Al alloy anodes enable improved cycling at lower N/P ratios, which is beneficial for energy density. This work provides insights into understanding the failure modes in Al alloy anodes.

Overall, cell design is integral to the microstructural evolution and capacity loss of Al alloy foil anodes. Alloying with amounts as low as 1 wt% strongly influences the resulting microstructure. Not only does the mode of degradation vary, but the LiAl island size is also composition dependent. Understanding the effects on the microstructural evolution by varying the alloying content in binary Al alloy foils, whether the element is active in the lithiation process, and the effect of various formation conditions should be studied. Under practical conditions, it has been shown that high additions of alloying elements can remain inactive, resulting in a decrease in energy density. Future work should focus on understanding the relationship between foil processing, cell design, and the impact on the resulting microstructure in other Al binary alloys, which can lay the groundwork for design strategies in multicomponent Al alloys.

Author contributions

C. T. designed and carried out the experiments, and A. M. supervised the work. Both authors wrote the manuscript.

Conflicts of interest

There are no conflicts to declare.

Data availability

The data supporting this article have been included as part of the supplementary information (SI). Any additional information is available from the authors upon request. Supplementary information is available. See DOI: https://doi.org/10.1039/d6ta00897f.

Acknowledgements

This work was supported by the National Science Foundation, Division of Chemical, Bioengineering, Environmental and Transport Systems under award number 2321486. One of the authors (C. T.) thanks the National Science Foundation Graduate Research Fellowship Program (NSF GRFP) for the award of the fellowship. The authors would like to thank Dr Eric Taleff for sharing their metallurgical expertise and valuable discussions.

References

1 W. Li, E. M. Erickson and A. Manthiram, *Nat. Energy*, 2020, **5**, 26–34.
2 L. Usai, J. J. Lamb, E. Hertwich, O. S. Burheim and A. H. Strømman, *Environ. Res. Infrastruct. Sustain.*, 2022, **2**, 011002.
3 W. Liu, P. Oh, X. Liu, M. Lee, W. Cho, S. Chae, Y. Kim and J. Cho, *Angew. Chem., Int. Ed.*, 2015, **54**, 4440–4457.
4 M. N. Obrovac and V. L. Chevrier, *Chem. Rev.*, 2014, **114**, 11444–11502.
5 B. T. Heligman and A. Manthiram, *ACS Energy Lett.*, 2021, **6**, 2666–2672.
6 T. Zheng and S. T. Boles, *Prog. Energy*, 2023, **5**, 032001.
7 S. Chen, C. Liu, R. Feng, Z. Chen, Y. Lu, L. Chen, Q. Huang, Y. Guan, W. Yan, Y. Su, N. Li and F. Wu, *Chem. Eng. J.*, 2025, **503**, 158116.
8 J. Asenbauer, T. Eisenmann, M. Kuenzel, A. Kazzazi, Z. Chen and D. Bresser, *Sustain. Energy Fuels*, 2020, **4**, 5387–5416.
9 M. N. Obrovac, L. Christensen, D. B. Le and J. R. Dahn, *J. Electrochem. Soc.*, 2007, **154**, A849.
10 T. Zheng, J. Zhang, X. Guo, W. Jin and S. T. Boles, *Electrochim. Acta*, 2024, **485**, 144127.
11 S. T. Boles and M. H. Tahmasebi, *Joule*, 2020, **4**, 1342–1346.
12 D. Li, F. Chu, Z. He, Y. Cheng and F. Wu, *Mater. Today*, 2022, **58**, 80–90.
13 A. Merrill, *Aluminum in June 2025*, U.S. Geological Survey, 2025.
14 T. Zheng and S. T. Boles, *ACS Omega*, 2022, **7**, 37867–37872.
15 Y. Liu, R. Zhang, J. Wang and Y. Wang, *iScience*, 2021, **24**, 102332.
16 J. X. Johnson, C. A. McMillan and G. A. Keoleian, *J. Ind. Ecol.*, 2013, **17**, 700–711.
17 H. Wang, H. Tan, X. Luo, H. Wang, T. Ma, M. Lv, X. Song, S. Jin, X. Chang and X. Li, *J. Mater. Chem. A*, 2020, **8**, 25649–25662.
18 Y. Liu, N. S. Hudak, D. L. Huber, S. J. Limmer, J. P. Sullivan and J. Y. Huang, *Nano Lett.*, 2011, **11**, 4188–4194.
19 T. Zheng, D. Kramer, M. H. Tahmasebi, R. Mönig and S. T. Boles, *ChemSusChem*, 2020, **13**, 5910–5920.
20 W.-J. Zhang, *J. Power Sources*, 2011, **196**, 13–24.
21 P. J. Crowley, K. P. Scanlan and A. Manthiram, *J. Power Sources*, 2022, **546**, 231973.
22 J. Zhang, T. Zheng, K. Lam and S. T. Boles, *Electrochim. Acta*, 2023, **456**, 142437.
23 X. Liu, Q. Zhu, A. Jiang, J. Yue, D. Yu, S. Wang, S. Dong, J. Zhao, W. Wang, S. Lyu, J. Wang, L. Shi, Y. Guo, W. Song, Y. Liu, J. Nai, R. Wang and H. Wang, *Adv. Funct. Mater.*, 2025, e21637.
24 H. Li, S. Nishimura, Y. Nakata, S. Matsumoto, T. Yamaguchi, H. Hoshikawa, T. Kumagai and T. Ichitsubo, *J. Mater. Chem. A*, 2023, **11**, 23311–23318.
25 H. T. Jeong, J. Jang, D. G. Lee, D. Lee and W. J. Kim, *J. Alloys Compd.*, 2023, **965**, 171279.
26 H. Li, T. Yamaguchi, S. Matsumoto, H. Hoshikawa, T. Kumagai, N. L. Okamoto and T. Ichitsubo, *Nat. Commun.*, 2020, **11**, 1584.
27 H.-T. Jeong and W. J. Kim, *ACS Appl. Mater. Interfaces*, 2024, **16**, 13662–13673.
28 L. Yang, W. Zhao, S. Sun, C. Xu, H. Sun, X. Zhang and G. Wang, *Mater. Today Commun.*, 2023, **37**, 107179.
29 T. Zheng, D. Kramer, M. H. Tahmasebi, R. Mönig and S. T. Boles, *ChemSusChem*, 2020, **13**, 974–985.
30 C. Trejo, K. Scanlan and A. Manthiram, *J. Electrochem. Soc.*, 2024, **171**, 040539.
31 C. Trejo, K. Scanlan and A. Manthiram, *J. Power Sources*, 2025, **653**, 237783.
32 C. Xu, Y. Wang, S. Sun, S. King, M. S. Kurbanov, X. Zhang and G. Wang, *ACS Sustainable Chem. Eng.*, 2024, **12**, 17018–17025.
33 X. Chen, F. Yang, C. Zhang, W. Wan, G. Liu, G. Qu, Z. Wang, S. Li, Y. Huang and C. Wang, *Adv. Energy Mater.*, 2024, **14**, 2304097.
34 E. L. Bray, *Magnesium Metal*, U.S. Geological Survey, 2025.
35 E. Schnebele, *Silicon*, U.S. Geological Survey, 2025.
36 H. Li, S. Nishimura, W. Liu, N. L. Okamoto, S. Matsumoto, Y. Nakata, H. Hoshikawa, T. Kumagai, T. Yamaguchi and T. Ichitsubo, *J. Mater. Chem. A*, 2025, **13**, 5723–5731.
37 H. T. Jeong and W. J. Kim, *J. Alloys Compd.*, 2025, **1016**, 178962.
38 T. S. Chen, C. Wang, S. C. Wright, K. A. Cavallaro, W. J. Jeong, S. Das, D. Majumdar, R. Gopalaswamy and M. T. McDowell, *PRX Energy*, 2024, **3**, 043005.
39 K. Scanlan and A. Manthiram, *J. Electrochem. Soc.*, 2023, **170**, 100515.
40 S. S. Sharma, P. J. Crowley and A. Manthiram, *ACS Sustainable Chem. Eng.*, 2021, **9**, 14515–14524.
41 T. Chen, A. C. Thenuwara, W. Yao, S. E. Sandoval, C. Wang, D. H. Kang, D. Majumdar, R. Gopalaswamy and M. T. McDowell, *Batter. Supercaps*, 2023, **6**, e202200363.
42 J. L. Murray and A. J. McAlister, *Bull. Alloy Phase Diagrams*, 1984, **5**, 74–84.
43 J. L. Murray, *Bull. Alloy Phase Diagrams*, 1982, **3**, 60–74.
44 J. L. Murray, *Int. Met. Rev.*, 1985, **30**, 211–234.
45 F. C. Campbell, in *Elements of Metallurgy and Engineering Alloys*, A S M International, 1st edn, 2008, pp. 487–508.
46 I. Balkanov and Y. Geronov, *J. Power Sources*, 1988, **24**, 71–79.
47 Y. Yu, S. Li, H. Fan, H. Xu, M. Jiang, Y. Huang and J. Li, *Nano Energy*, 2020, **67**, 104274.
48 H. Li, L. Wang, Y. Song, Z. Zhang, H. Zhang, A. Du and X. He, *Adv. Funct. Mater.*, 2023, **33**, 2305515.
49 T. Zheng, D. Kramer, R. Mönig and S. T. Boles, *ACS Sustainable Chem. Eng.*, 2022, **10**, 3203–3210.
50 R. A. Huggins, *J. Power Sources*, 1999, **81–82**, 13–19.
51 Y. Guo, D. Li, Z. Zhao, M. Tang, L. Dong, J. Zhan, Q. Li and F. Wu, *Adv. Energy Mater.*, 2025, e04817.
52 J. B. Adamo and A. Manthiram, *Chem. Mater.*, 2024, **36**, 6226–6236.
53 J. B. Cook, H.-S. Kim, T. C. Lin, S. Robbennolt, E. Detsi, B. S. Dunn and S. H. Tolbert, *ACS Appl. Mater. Interfaces*, 2017, **9**, 19063–19073.

54 X. Zhang, W. Zhao, J. Cai, C. Xu, S. Chen, G. Chen and G. Wang, *Solid State Ionics*, 2022, **387**, 116081.
55 R. Tan, J. Zhang, K. Liu, X. Zhu, R. Gao, Q. Zhang, Y. Wang, X. Ai and J. Qian, *Adv. Funct. Mater.*, 2024, **34**, 2316341.
56 M. Zhang, L. Xiang, M. Galluzzi, C. Jiang, S. Zhang, J. Li and Y. Tang, *Adv. Mater.*, 2019, **31**, 1900826.
57 L. Y. Beaulieu, K. W. Eberman, R. L. Turner, L. J. Krause and J. R. Dahn, *Electrochem. Solid-State Lett.*, 2001, **4**, A137.
58 V. Guterman, Yu. Averina and V. Grigor'ev, *Electrochim. Acta*, 1999, **45**, 873–880.
59 H.-T. Jeong and W. J. Kim, *ACS Energy Lett.*, 2025, 5834–5856.
60 A.-J. Mohammed, I. Maher, M. Nakai and M. A. H. Gepreel, *Mater. Today: Proc.*, 2023, S2214785323048101.
61 C. Wang, T. Chen, Y. Liu, D. H. Kang, D. Majumdar, R. Gopalaswamy and M. T. McDowell, *ACS Energy Lett.*, 2023, **8**, 2252–2258.
62 M. H. Tahmasebi, D. Kramer, R. Mönig and S. T. Boles, *J. Electrochem. Soc.*, 2019, **166**, A5001–A5007.
63 K.-Y. Park, J.-W. Park, W. M. Seong, K. Yoon, T.-H. Hwang, K.-H. Ko, J.-H. Han, Y. Jaedong and K. Kang, *J. Power Sources*, 2020, **468**, 228369.
64 J. Vetter, P. Novák, M. R. Wagner, C. Veit, K.-C. Möller, J. O. Besenhard, M. Winter, M. Wohlfahrt-Mehrens, C. Vogler and A. Hammouche, *J. Power Sources*, 2005, **147**, 269–281.
65 B. T. Heligman, K. P. Scanlan and A. Manthiram, *J. Electrochem. Soc.*, 2021, **168**, 120544.
66 A. Ch. Lazanas and M. I. Prodromidis, *ACS Meas. Sci. Au*, 2023, **3**, 162–193.
67 B. T. Heligman, K. J. Kreder and A. Manthiram, *Joule*, 2019, **3**, 1051–1063.
68 B. T. Heligman, K. P. Scanlan and A. Manthiram, *ACS Appl. Mater. Interfaces*, 2022, **14**, 11408–11414.
69 H.-T. Jeong and W. J. Kim, *Mater. Horiz.*, 2026, **13**, 1850–1865.
70 H. Fan, B. Chen, S. Li, Y. Yu, H. Xu, M. Jiang, Y. Huang and J. Li, *Nano Lett.*, 2020, **20**, 896–904.